Interactions between a cavitation bubble and solidification front under the effects of ultrasound: Experiments and lattice Boltzmann modeling

Yu Chen [a], Qingyu Zhang [a,*], Xiaonan Wang [a], Zhengjun Yao [b,c]

[a] *School of Iron and Steel, Soochow University, Suzhou 215137, China*
[b] *College of Materials Science and Technology, Nanjing University of Aeronautics and Astronautics, Nanjing 211100, China*
[c] *Key Laboratory of Materials Preparation and Protection for Harsh Environment, Ministry of Industry and Information Technology, Nanjing 211106, China*

ARTICLE INFO

ABSTRACT

The phenomena of melting and dendritic fragmentation are captured by using an *in-situ* device during the ultrasound-assisted solidification of a succinonitrile-acetone (SCN-ACE) alloy. The experimental results show that the dendrite arms detach from primary trunk due to the melting of the solid phase, which is caused by a moving ultrasound cavitation bubble. To quantify the interactions between the ultrasound cavitation bubble and the solidification front, a coupled lattice Boltzmann (LB) model is developed for describing the fields of temperature, flow, and solid fraction, and their interactions. The multi-relaxation-time (MRT) scheme is applied in the LB model to calculate the liquid-gas flow field, while the Bhatnagar–Gross–Krook (BGK) equation is executed to simulate the evolution of temperature. The kinetics of solidification and melting are calculated according to the lever rule based on the SCN-ACE phase diagram. After the validation of the LB model by an analytical model, the morphologies of the cavitation bubble and solidification front are simulated. It is revealed that the solidification interface melts due to the increase of the temperature nearby the cavitation bubble in ultrasonic field. The simulated morphologies of the cavitation bubble and solidification front are compared well with the experimental micrograph. Quantitative investigations are carried out for analyzing the melting rate of the solidification front under different conditions. The simulated data obtained from LB modeling and theoretical predictions reasonably accord with the experimental results, demonstrating that the larger the ultrasonic intensity, the faster the melting rate. The present study not only reveals the evolution of the solidification front shape caused by the cavitation bubbles, which is invisible in the ultrasound-assisted solidification process of practical alloys, but also reproduces the complex interactions among the temperature field, acoustic streaming, and multi-phase flows.

1. Introduction

Ultrasonic wave is widely applied in the solidification of metallic alloy for microstructure refinement [1–3]. The proposed mechanisms of grain refinement induced by ultrasound can be summarized into two categories: (1) Enhancement of homogenous and/or heterogeneous nucleation [4–6]. The homogeneous grain nucleation is due to the increased melting point of the material around the cavitation bubbles generated by ultrasound, while the heterogeneous nucleation is because the wettability of impurity particles is improved in the melt. (2) Fragmented dendrites caused by ultrasound acting as new grain seeds [7–9]. The fragmented dendrites are produced for many reasons, such as the local melting of the dendrite root caused by solute enrichment or by heat

flows, together with strong forces caused by the variation of acoustic pressure.

The process of dendritic fragmentation in ultrasound-assisted solidification has been captured recently by *in-situ* experiments of transparent organic alloys [2,7,10,11] or real metallic alloys [8,12,13]. Shu et al. [7] investigated the interactions of cavitation bubbles and succinonitrile dendrites in the ultrasonic field with a high-speed camera. The results revealed that the cavitation bubble collapse generated disordered flows, resulting in sufficient forces to fracture the roots of dendrite arms. Wang et al. [2] captured the behavior of dendrite melting and cavitation bubble oscillation using a high-speed camera. A theoretical model has been proposed to demonstrate that the pressure generated by cavitation bubbles has a significant influence on the fragmentation of the dendrite.

Nagira et al. [12] investigated the behavior of the dendritic microstructure with Sb-based alloys under effects of ultrasound adopting X-ray radiography. They found that the dendrites immediately detached after the ultrasonic device worked. This is because the solute enriches in the mushy region due to the flow caused by ultrasonic waves, which leads to local remelting and thus separates the dendrite arms. Wang et al. [8] applied high-speed synchrotron X-ray radiography to study the solidification of aluminum alloys assisted by high-intensity ultrasonic vibrations. The results indicated that the fragmented mechanisms of dendrites mainly are the local remelting owing to the hot liquid transported by disordered flow appeared in the dendrites, and the stress acting on the dendrites. It can be derived from the above studies that the phenomena of dendritic fragmentation are related to the melting of the solid phase caused by the ultrasound cavitation bubble. Although the experiments can provide a lot of important information on solid melting and dendritic fragmentation, the physics underneath the interaction among the phase transformation, temperature field, acoustic streaming, and ultrasonic cavitation bubbles still remains ambiguous.

With the development of computer science over the decades, numerical modeling has become a critical method to study the microstructure of solidification assisted by external fields. [14]. Due to the facts that the cavitation bubbles appear in the liquid and directly affect the growing dendrites or planar interface during the ultrasound-assisted solidification process, it is essential to find a reliable fluid model for simulating the solid-liquid-gas coexisting systems. Recently, the lattice Boltzmann (LB) models, having the merits of simple algorithm and high parallel computational efficiency, have received great attention in the fields related to ultrasound research [15]. The LB models treat fluids as the collection of discrete pseudoparticles, and the evolution of macroscopic flow can be described through the migration and collision processes of the pseudoparticles [16]. Shan et al. [15] developed the LB model for simulating the pressure in liquid under ultrasound. The simulated pressure is consistent with the measured results.

In this work, a coupled LB model is developed for the investigation of the interactions between the solidification front and the ultrasonic cavitation bubble. *In situ* observations of the melting of solidification front of a succinonitrile-acetone alloy, caused by the cavitation bubble, are carried out. The melting phenomena of the solidification front are analyzed through the comparisons of theoretical model, LB simulation, and experimental results.

2. Model description and governing equations

The purpose of this work is to investigate the interactions between the melting of solidification front and cavitation bubbles induced by ultrasound in directional solidification of a SCN-1.65wt. %ACE alloy.

The multi-relaxation-time (MRT) scheme is implemented in the LB model to simulate the liquid-gas flows. The MRT LB equation is written as [14,17].

$$f_i(\mathbf{x} + \mathbf{e}_i\Delta t, t + \Delta t) - f_i(\mathbf{x}, t) = -\left(\mathbf{M}^{-1}\mathbf{\Lambda}\mathbf{M}\right)_{ij}\left(f_j - f_j^{eq}\right) + F_i'\Delta t$$
$$i, j = 0, 1, \ldots, 8 \tag{1}$$

where f_i is the density distribution function and f_i^{eq} represents its equilibrium distribution function. $\mathbf{x}$ is the spatial position, $\mathbf{e}_i$ represents the discrete velocities along the ith direction and Δt represents the time step in the LB model. F_i' is the forcing term. $\mathbf{M}$ and $\mathbf{M}^{-1}$ are orthogonal transformation matrices and the corresponding inverse matrix, $\mathbf{M}$ is defined by

$$M = \begin{bmatrix} 1 & 1 & 1 & 1 & 1 & 1 & 1 & 1 & 1 \\ -4 & -1 & -1 & -1 & -1 & 2 & 2 & 2 & 2 \\ 4 & -2 & -2 & -2 & -2 & 1 & 1 & 1 & 1 \\ 0 & 1 & 0 & -1 & 0 & 1 & -1 & -1 & 1 \\ 0 & -2 & 0 & 2 & 0 & 1 & -1 & -1 & 1 \\ 0 & 0 & 1 & 0 & -1 & 1 & 1 & -1 & -1 \\ 0 & 0 & -2 & 0 & 2 & 1 & 1 & -1 & -1 \\ 0 & 1 & -1 & 1 & -1 & 0 & 0 & 0 & 0 \\ 0 & 0 & 0 & 0 & 0 & 1 & -1 & 1 & -1 \end{bmatrix} \tag{2}$$

$\mathbf{\Lambda}$ is a diagonal matrix, and the different relaxation times lie on the diagonal of $\mathbf{\Lambda}$, which is given by

$$\mathbf{\Lambda} = diag\left(\tau_\rho^{-1}, \tau_e^{-1}, \tau_\zeta^{-1}, \tau_j^{-1}, \tau_q^{-1}, \tau_j^{-1}, \tau_q^{-1}, \tau_\nu^{-1}, \tau_\nu^{-1}\right) \tag{3}$$

where the values of the relaxation times are set to be $\tau_\rho = \tau_j = \tau_\nu = 1.0$, $\tau_e = \tau_\zeta = 5/4$, $\tau_q = 10/11$, respectively.

Based on the computation of the liquid kinematic viscosity in the LB model and in the physical word, the physical time of each LB time step is calculated by

$$\Delta t = \Delta x^2 \cdot \frac{(\tau_\nu - 0.5)/3}{\mu/\rho_0} \tag{4}$$

where Δx is the physical lattice spacing, and $\Delta x = 2\ \mu m$ are fixed in the present work. μ represents the viscosity of liquid, and ρ_0 is initial density of SCN. The numerator and denominator of Eq. (4) represent the kinematic viscosities of liquid in the LB and physical units, respectively.

The discrete velocities in Eq. (1), $\mathbf{e}_i$, are written in matrix forms as follows:

$$[e_0, e_1, e_2, e_3, e_4, e_5, e_6, e_7, e_8] = c \cdot \begin{bmatrix} 0 & 1 & 0 & -1 & 0 & 1 & -1 & -1 & 1 \\ 0 & 0 & 1 & 0 & -1 & 1 & 1 & -1 & -1 \end{bmatrix} \tag{5}$$

where $c = \Delta x/\Delta t$ is the lattice speed.

In the LB model, the streaming of the liquid-gas particles is simulated in the velocity, while their collision is computed in the moment space. It is realized that the density distribution function $\mathbf{f}$ and its equilibrium function $\mathbf{f}^{eq}$ can be transformed from the velocity space into the moment space *via* $\mathbf{m} = \mathbf{Mf}$ and $\mathbf{m}^{eq} = \mathbf{Mf}^{eq}$, respectively. $\mathbf{m}^{eq}$ can be given by

$$m^{eq} = \rho\left[1, -2 + 3|\mathbf{u}|^2, 1 - 3|\mathbf{u}|^2, u_x, -u_x, u_y, -u_y, u_x^2 - u_y^2, u_x u_y\right]^T \tag{6}$$

where the macroscopic density, ρ, can be calculated by accumulating the density, which is given by $\rho = \sum_{i=0}^8 f_i$. And then the velocity, $\mathbf{u}$, of the particles is computed by $\mathbf{u} = \left(\sum_{i=0}^8 \mathbf{e}_i f_i + \mathbf{F}\Delta t/2\right)\Big/\rho$, where $\mathbf{F}$ is the resultant force acting on the particles including the intermolecular interaction force, $\mathbf{F}_c$, and the fluid-solid adhesion force, $\mathbf{F}_w$. $\mathbf{F}_c$ and $\mathbf{F}_w$ are calculated by

$$\mathbf{F}_c(\mathbf{x}, t) = -G_c\psi(\mathbf{x}, t)\sum_{i=0}^8 \omega_i\psi(\mathbf{x} + \mathbf{e}_i\Delta t, t)\mathbf{e}_i \tag{7}$$

$$\mathbf{F}_w(\mathbf{x}, t) = -G_w\psi^2(\mathbf{x}, t)\sum_{i=0}^8 \omega_i s(\mathbf{x} + \mathbf{e}_i\Delta t, t)\mathbf{e}_i \tag{8}$$

where G_c and G_w are the interaction strength and the adsorption parameter, respectively. In the present work, $G_c = -1$ and $G_w = -1.1$ are applied. $s(x + e_i\Delta t, t)$ is an indicator function, which is equal to 1 for a solid phase. Otherwise, its value is 0. The magnitudes of the forces induce phase segregation, which is defined *via* the pseudopotential function, ψ. In this model, ψ is taken as

$$\psi = \sqrt{2\left(P_{EOS} - \rho c_s^2\right)/G_c} \tag{9}$$

Table 1

Physical parameters employed in the current work.

Symbol	Definition and units	Value	Refs.
T_m	Melting point of the pure SCN (K)	331.23	[21]
m_l	Liquidus slope (K·wt%$^{-1}$)	−2.971	[21]
c_0	Initial composition (wt%)	1.65	–
k_p	Partition coefficient of solute	0.124	[21]
μ	Viscosity of liquid (Pa·s)	1.44×10^{-3}	[22]
ρ_0	Density of SCN (kg·m^{-3})	970	[23]

where P_{EOS} is an equation of state which is written by Peng-Robinson [18].

$$P_{EOS} = \frac{\rho R T_R}{1 - b\rho} - \frac{a\alpha(T)\rho^2}{1 + 2b\rho - b^2\rho^2} \tag{10}$$

where R is equal to 1. a represents the attraction parameter and b is the repulsion parameter, and a and b are set to be 2/49 and 2/21, respectively. T_R is set to be $T_R = 0.8*T_c$, and $\alpha(T)$ is defined by $\alpha(T) = \left[1 + \left(0.37464 + 1.5226\omega - 0.26992\omega^2\right) \times \left(1 - \sqrt{T/T_c}\right)\right]^2$, where T_c is equal to 0.072922 and ω is set to be 0.344.

After Eq. (2) and Eq. (3) are introduced into Eq. (1), which becomes

$$\boldsymbol{m}^* = \boldsymbol{m} - \boldsymbol{\Lambda}(\boldsymbol{m} - \boldsymbol{m}^{eq}) + \Delta t(\mathbf{I} - 0.5\boldsymbol{\Lambda})\boldsymbol{S} \tag{11}$$

where $\mathbf{I}$ is the unit tensor, and $\boldsymbol{S}$ represents the forcing term in the moment space, which is derived by $\mathbf{MF}' = (\mathbf{I} - 0.5\boldsymbol{\Lambda})\boldsymbol{S}$. In the present model, $\boldsymbol{S}$ is defined by

$$\boldsymbol{S} = \begin{bmatrix} 0 \\ 6u\cdot\boldsymbol{F} + 12\varepsilon|\boldsymbol{F}|^2/\left(\psi^2\Delta t(\tau_e - 0.5)\right) \\ -6u\cdot\boldsymbol{F} - 12\varepsilon|\boldsymbol{F}|^2/\left(\psi^2\Delta t(\tau_\zeta - 0.5)\right) \\ F_x \\ -F_x \\ F_y \\ -F_y \\ 2\left(u_x F_x - u_y F_y\right) \\ u_x F_y + y_y F_x \end{bmatrix} \tag{12}$$

where $\varepsilon = 0.09$ is set to keep the stability of model.

The streaming process of the liquid-gas particles is given as

$$f_i(\mathrm{x} + \mathrm{e}_i\Delta t, t + \Delta t) = f_i^*(\mathrm{x}, t) \tag{13}$$

where f^* can be obtained by $\boldsymbol{f}^* = \mathbf{M}^{-1}\boldsymbol{m}^*$.

The Bhatnagar–Gross–Krook (BGK) LB scheme is employed to calculate the evolution of the temperature field. The evolution of the temperature distribution function, $T_i(\boldsymbol{x}, t)$, can be written as

$$T_i(\boldsymbol{x} + \boldsymbol{e}_i\Delta t, t + \Delta t) - T_i(\boldsymbol{x}, t) = -\frac{1}{\tau}\left(T_i(\boldsymbol{x}, t) - T_i^{eq}(\boldsymbol{x}, t)\right)$$

$$i, j = 0, 1, \ldots, 8 \tag{14}$$

where τ is the relaxation time, which is related to the heat diffusivity of the SCN-ACE melt. $T_i^{eq}(\boldsymbol{x}, t)$ represents the equilibrium distribution function used in the temperature evolution computation. The local temperature can be calculated by $T = \sum_{i=0}^{8} T_i$.

In Eq. (14), $T_i^{eq}(\boldsymbol{x}, t)$ is calculated by.

$$T_i^{eq}(\mathrm{x}, t) = \omega_{c,i} T(\boldsymbol{x}, t)\left(1 + 3\frac{\boldsymbol{e}_i\cdot\boldsymbol{u}(\boldsymbol{x}, t)}{c^2} + 4.5\frac{(\boldsymbol{e}_i\cdot\boldsymbol{u}(\boldsymbol{x}, t))^2}{c^4} - 1.5\frac{(\boldsymbol{u}(\boldsymbol{x}, t))^2}{c^2}\right) \tag{15}$$

where $\omega_{c,i}$ are the weight coefficients for the calculation of temperature filed, given by $\omega_{c,0} = 4/9$, $\omega_{c,1-4} = 1/9$, and $\omega_{c,5-8} = 1/36$, respectively.

After each step of the LB calculations, the positions of temperature and density in computation domain evolve. According to the temperature of each node, T, the local solid fraction, f_s, is calculated through the lever rule based on the equilibrium SCN-ACE phase diagram,

$$f_s = \frac{\left((T - T_m)/m_l - c_0\right)}{(T - T_m)/m_l - (T - T_m)\cdot k_p/m_l} \tag{16}$$

where T_m is the melting temperature of pure SCN. m_l, c_0, and k_p are the liquidus slope, initial composition, and solute partition coefficient, respectively. Therefore, the solidification and melting phenomena are incorporated in the LB model according to Eq. (16).

In order to simulate the ultrasonic streaming, a certain part of the west boundary of the computation domain is assumed to be a source producing the ultrasonic wave, in which the velocity of the ultrasound source is calculated by [19].

$$u_{stream} = A\sin(2\pi f_p t) \tag{17}$$

where A represents the amplitudes of the velocity variations, f_p is the frequency of the ultrasound wave, and t represents the physical time.

The periodic boundary condition is used in the MRT LB model for simulating the liquid-gas flows, while the nonequilibrium extrapolation boundary condition is applied on the west and east walls of the domain for calculating the temperature field. A bounce-back rule is implemented on the fluid-solid interface.

The nonequilibrium extrapolation boundary is expressed by [20].

$$T_i(\boldsymbol{x}_b, t) = T_i^{eq}(\boldsymbol{x}_b, t) + T_i^{neq}(\boldsymbol{x}_b, t)$$
$$= T_i^{eq}\left(T_b, \boldsymbol{u}(\boldsymbol{x}_f)\right) + \left(T_i(\boldsymbol{x}_f) - T_i^{eq}(\boldsymbol{x}_f)\right) \tag{18}$$

where T_i^{eq} and T_i^{neq} represent the equilibrium and nonequilibrium distribution functions, respectively. $\boldsymbol{x}_b$ and $\boldsymbol{x}_f$ are the positions of the boundary and the adjacent fluid nodes, which have the relationship of $\boldsymbol{x}_b = \boldsymbol{x}_f + \boldsymbol{e}_i\Delta t$. T_b is the temperature at the boundary.

The physical parameters employed in the current work are shown in Table 1.

3. Experimental

The directional solidification experiments assisted by ultrasound with transparent SCN-1.65 wt% ACE alloy are implemented by adopting a Bridgman-type solidification setup that can observe the real-time process of solidification. The schematic diagram of the *in situ* experimental setup is displayed in Fig. 1. A rectangular glass tube produced by Vitrocom with product model 3524 is filled with the SCN-1.65 wt% ACE melt. The glass tube is placed on a horizontal pulling strip connecting to a moving device. The glass tube is located at the gap between the copper plates connecting the high-temperature and low-temperature water baths, and the gap width is 10 mm. Thus, a stable temperature gradient is formed at the gap. The experimental process is divided into two parts. First, the moving device is set to move to the cold copper plate with a velocity of $V_p = 100\ \mu m\cdot s^{-1}$. The pulling strip drives the glass tube to move at the same speed. As a result, columnar dendrites form in the tube. The pulling is stopped after the columnar crystals grow steadily. After holding of the sample for a while in the temperature gradient, a planar solidification front is produced due to the effects of temperature gradient zone melting [24]. The ultrasonic equipment is turned on and the ultrasonic horn touches the glass tube. It is worth noting that a relatively higher ultrasonic intensity should be applied to ensure the existence of the cavitation bubbles in the glass tube. The interactions between cavitation bubbles and solidification front inside the glass tube are captured by an optical microscope. The images are captured by a CCD camera that is connected to a computer, and the computer saves the images through professional software.
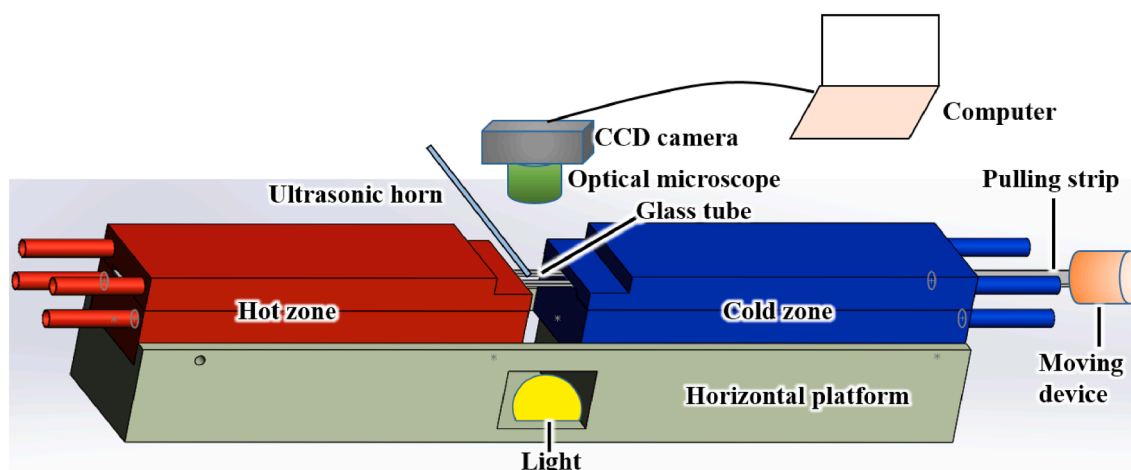
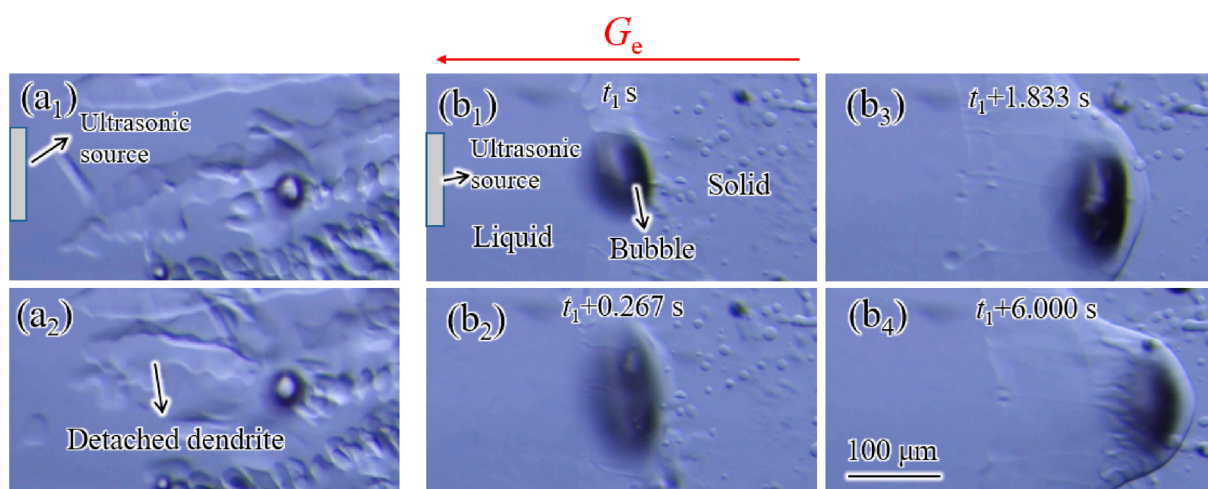**Fig. 1.** Schematic diagram of the *in situ* experimental setup.

Fig. 2. Process of dendrite detachment (a) and the melting of the solidification front caused by the ultrasound cavitation bubble (b). The horizontal red arrow above represents the direction of temperature gradient.
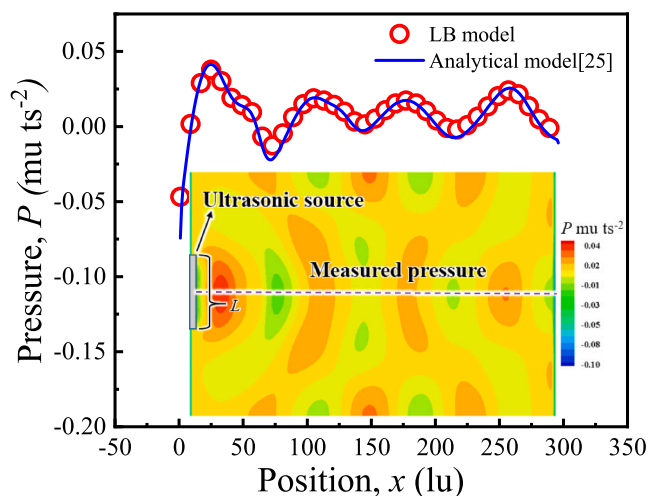

Fig. 3. Comparison of the pressure data obtained from the LB model and the analytical model [25] in the center of liquid domain at the time steps of 30,000. The inserted picture displays the simulated flow of ultrasonic waves, where the position of the measured pressure is at the dashed line, L is the length of the ultrasonic source.

4. Results and discussion

4.1. In situ observation of the interactions between cavitation bubbles and solidification front

In the *in situ* experiment, the experimental temperature gradient, G_e, is kept constant at 4000 K·m^{-1}. The ultrasonic frequency is 20 kHz. The process of the dendrite fragmentation caused by the ultrasound cavitation bubbles can be observed in Fig. 2a$_1$ and a$_2$. It can be found that the solid phase around the gas bubble melts, which is the main reason inducing the dendritic detachment. In order to further understand the melting of the solid phase, the evolution of a cavitation bubble interacting with a planar solidification front is investigated by experiments. As shown in Fig. 2b$_1$-b$_4$, a cavitation bubble having the size of about 100 µm is generated in liquid due to the varying pressure caused by the ultrasound, and then the cavitation bubble moves along the direction that is opposite to the temperature gradient (see the red arrow showing the temperature gradient direction). The moving cavitation bubble is blocked by the solidification front after applying ultrasound for several seconds. As a result, the cavitation bubble contacts the solid phase, which can be seen in Fig. 2b$_1$. It can be seen in Fig. 2b$_2$ and b$_3$ that the cavitation bubble oscillates with high frequency and the solid phase is melted. The cavitation bubble continuously moves to the right-hand side because of the convective flow in liquid caused by the ultrasound. It can
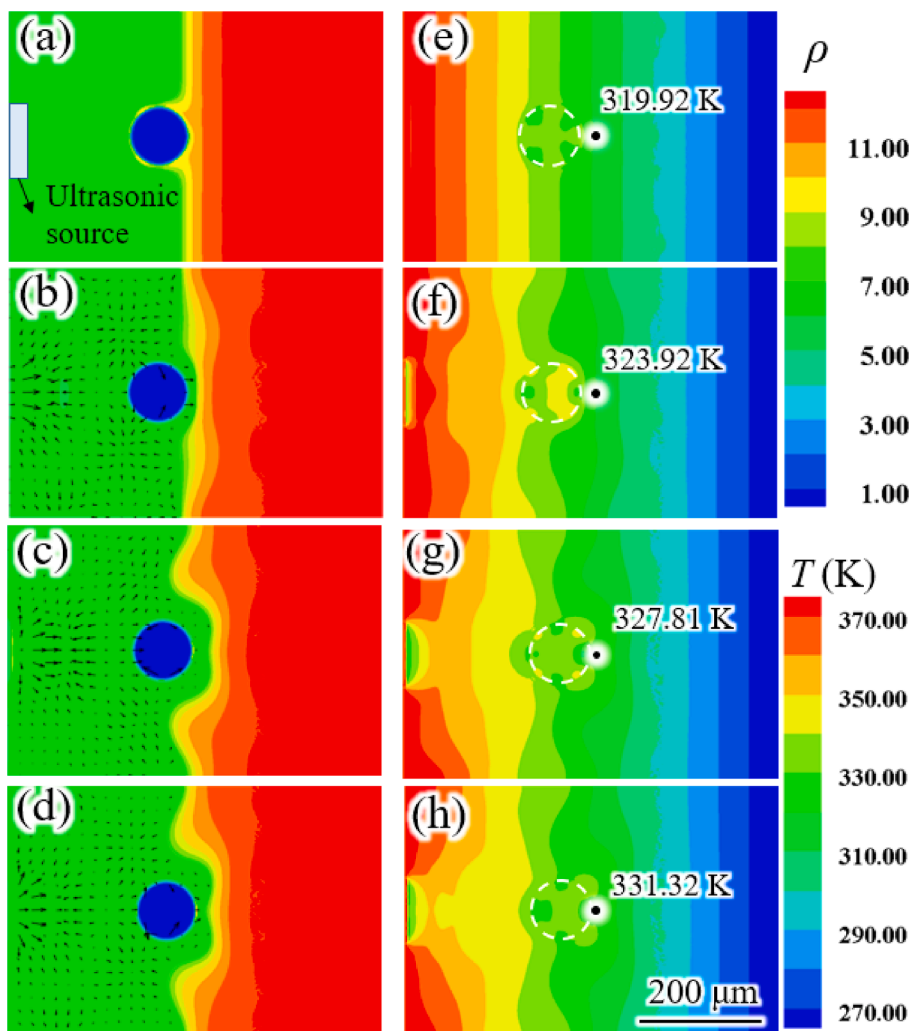
Fig. 4. Simulated evolution of morphology (a)-(d) and temperature (e)-(h) during the ultrasound-assisted directional solidification: (a, e) 0 Δt; (b, f) 23,000 Δt; (c, g) 100,000 Δt; (d, h) 176,000 Δt. The black arrows indicate the velocity vectors. The red, green, and blue represent the solid, liquid, and cavitation bubbles, respectively. The white circles represent the position of the cavitation bubble.

be speculated that the flow could facilitate heat exchange. Therefore, the solidified region is heated by high-temperature flow and the oscillation of the cavitation bubble also accelerates the flow, which causes the temperature around the cavitation bubble to increase. As a result, the solid melting takes place as long as the ultrasound is applied. The morphology of solidification front after sonication for several seconds is displayed in Fig. 2b₄. It can be seen that the cavitation bubble moves perpendicular to the propagation direction of the ultrasound in Fig. 2a₁ and a₂, while the cavitation bubble moves parallel to the ultrasound direction in Fig. 2b₁-b₄. It is because the interdendritic gap provides enough space for the movement of the cavitation bubble under the effects of the acoustic pressure in Fig. 2a₁ and a₂. However, in Fig. 2b₁-b₄ the cavitation bubble in the experiment of the planar interface is blocked by the solid, even if the acoustic pressure and streaming might have the strongest effects along the parallel direction.

4.2. Model validation of the LB model for the simulation of ultrasound propagation in liquid

Prior to the simulation of the interaction between the ultrasound cavitation bubble and solidification front, it is necessary to validate the correctness of the developed LB model for simulating the ultrasound propagation in liquid.

According to the work of Walsh and Torres [25], the pressure

distribution in fluid under the condition of ultrasound is calculated by

$$p = c_0^2(\rho - \rho_l) \tag{19}$$

where c_0^2 and ρ_l represent the square of the linear speed of sound and the initial density of liquid, respectively.

In this LB model, the computation domains consist of 300×200 lattice units (lu) with 1 lu = 1 Δx = 2 μm. The initial fluid density is $\rho_l = 7.179$. The left boundary is set to be the source of ultrasound with the length, $L = 50$ lu. The ultrasonic parameters are $f_p = 20,000$ and $A = 0.03$, respectively. After 30,000 steps, the comparison of the pressure data obtained from the LB modeling (Eq. (10)) and the analytical model (Eq. (19)) can be found in Fig. 3, where the inserted picture shows the simulated flow of ultrasonic waves. It is seen that the pressure fluctuates as the position departing from the ultrasonic source. Fig. 3 reveals that the pressure values obtained from the LB model superpose those calculated by the analytical model, demonstrating the correctness of the LB model for the simulation of ultrasound propagation in fluid.

4.3. Melting of the solidification front caused by an ultrasound cavitation bubble

The LB model is then used to simulate the interaction between cavitation bubbles and solidification front caused by ultrasonic waves.
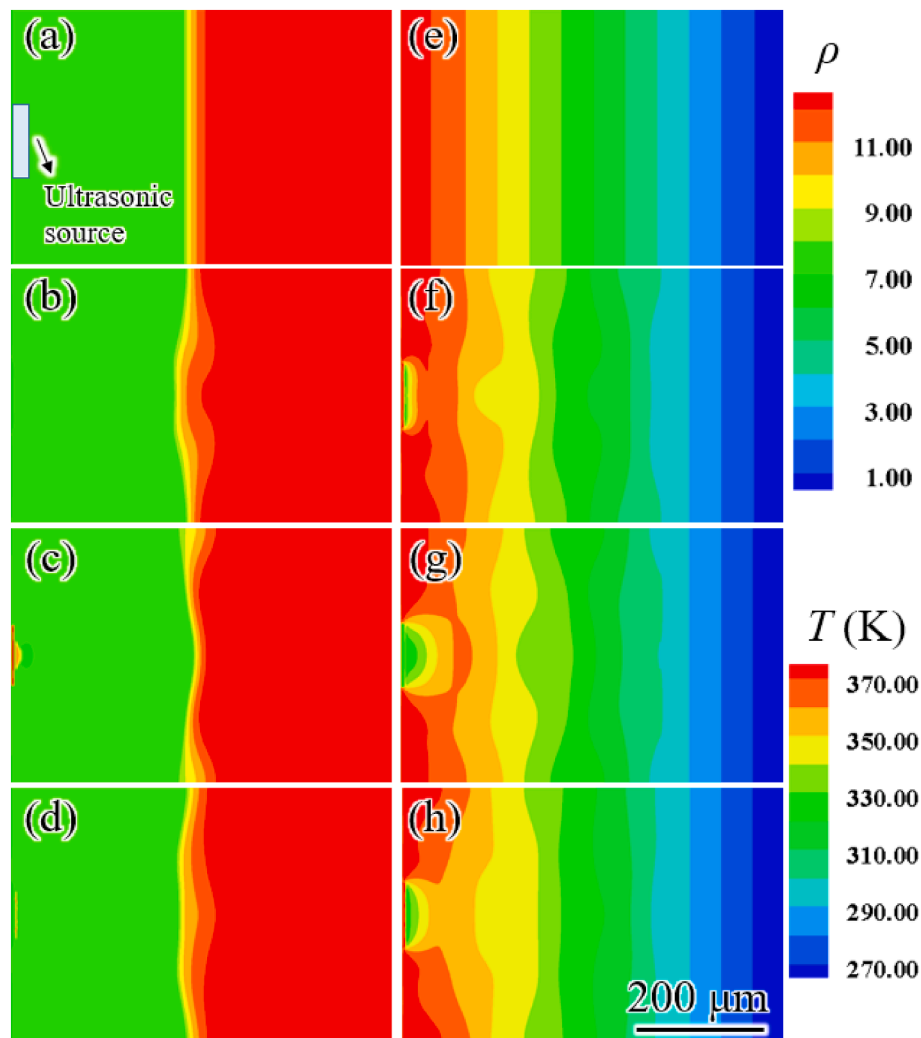
Fig. 5. Simulated evolution of morphology (a)-(d) and temperature (e)-(h) under the effects of the ultrasound without a cavitation bubble: (a, e) 0 Δt; (b, f) 10,000 Δt; (c, g) 50,000 Δt; (d, h) 80,000 Δt. The red and green colors represent the solid and liquid phases, respectively.
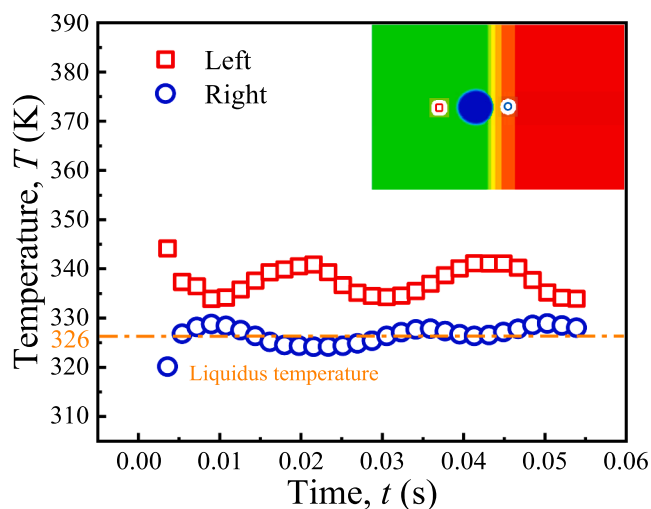

Fig. 6. Simulated temperature on the left and right-hand sides of cavitation bubble varying with the physical time for the case of Fig. 4. The inset shows the location of the two measured points.

The computation domains consist of 300 × 200 lu. The simulated temperature gradient, G_s is set to be 20,000 K·m^{-1}. The ultrasonic source with a 50 lu length is located at the west boundary. The temperature of the left boundary is set to be 380 K, which is above the liquidus temperature of the material. A cavitation bubble of radius with 25 lu contacts with the solid is placed in the domain. The evolution of morphology and temperature with ultrasonic time during the directional solidification is displayed in Fig. 4a-h, where Fig. 4a-d are shown in density field for representing the evolution of the solidification front morphology, and Fig. 4e-h are shown in temperature field. The red, green, and blue in Fig. 4a-d represent the solid, liquid, and cavitation bubbles, respectively. Fig. 4a shows the initial morphology of the gas-liquid-solid system, while Fig. 4e presents the initial temperature field. The temperature of nearby the cavitation bubble is 319.92 K (see the dot in Fig. 4e), which is below liquidus temperature, and thus it is the solid phase before the ultrasound is imposed. After the ultrasound is applied, the velocity vectors in liquid can be seen in Fig. 4b. It is obvious that the flow rate nearby the left boundary is larger because of the ultrasonic attenuation. The flow can affect the liquid density, which in turn affects the pressure distribution (see Eq. (19)). Therefore, the pressure also attenuates. The identical results can be found elsewhere [16,26]. The right direction of the velocity nearby the cavitation bubble denotes that the cavitation bubble is pushed by liquid. Fig. 4b shows that the cavitation bubble and the solidification front are no longer in contact, which indicates that the solidification front is melted simultaneously. As shown
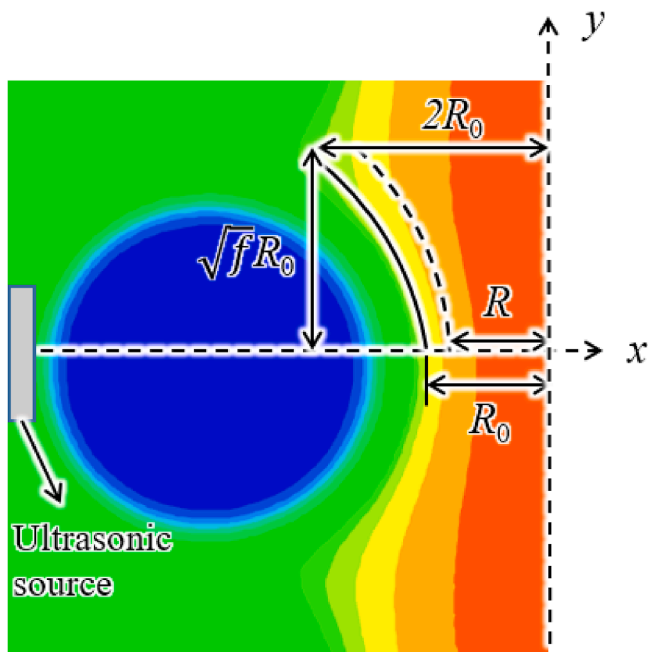
Fig. 7. Schematic illustration of the interactions between a cavitation bubble and solidification front.
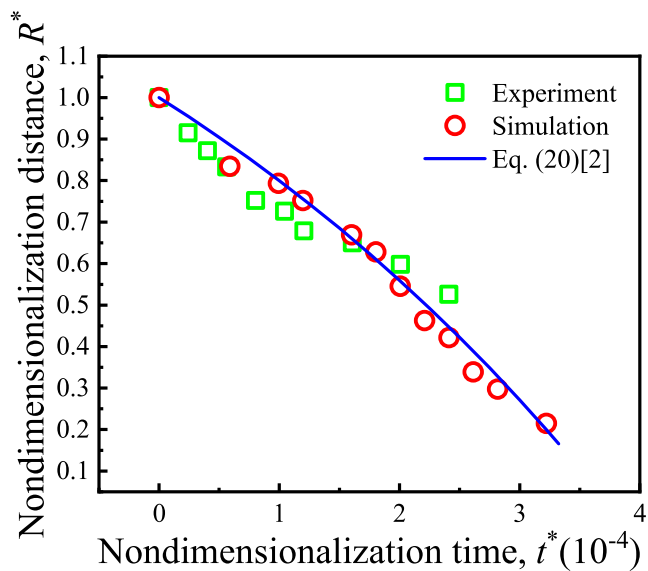

Fig. 8. Comparison of the melting distance of the solidification front obtained from the *in situ* experiments, LB simulations, and theoretical predictions [2] based on Fig. 2 and Fig. 4.

Fig. 9. Simulated evolutions of the distance between the right boundary and the solidification front, d with time step, Δt under different ultrasonic intensities.

Table 2
The factors of the theoretical model used in the present work.

Symbol	Definition and units	Value	Refs.
ΔS_f	Entropy of fusion (J•m^{-3}•K^{-1})	1.440×10^5	[2]
α_L	Thermal diffusion of liquid (m^2•s^{-1})	1.16×10^{-7}	[2]
C_L	Heat capacity of liquid (J·m^3•K^{-1})	1.920×10^6	[2]
γ_{sl}	Surface energy (J•m^{-2})	8.96×10^{-3}	[2]
LS_H	Latent/sensible heat (J·m^{-3})	4.769×10^7	[23]
f	Factor of shape	1.48	Calculated
R_0^*	Initial dimensionless distance	1	Calculated
ΔP^*	Dimensionless pressure difference	−1350	Calculated

in Fig. 4f, the temperature fluctuates near the ultrasonic source, while the temperature nearby the right boundary is still stable. The temperatures of the cavitation bubble and the dotted region increase under the effects of the ultrasonic source. However, the moving distance of the cavitation bubble driven by convective flow is not obvious due to the limited time. The position of the cavitation bubble and the symmetrical morphology of the solidification front have changed after the ultrasound works for a while (see Fig. 4c and g). The cavitation bubble moves to the position of the dotted region assisted by ultrasonic waves and the temperature there is 327.81 K which is higher than liquidus temperature. Thereafter, the melting takes place in the dotted region as shown in Fig. 4c and g. The cavitation bubble is then pushed to lower temperature regions and continues to melt the solidification front, which are
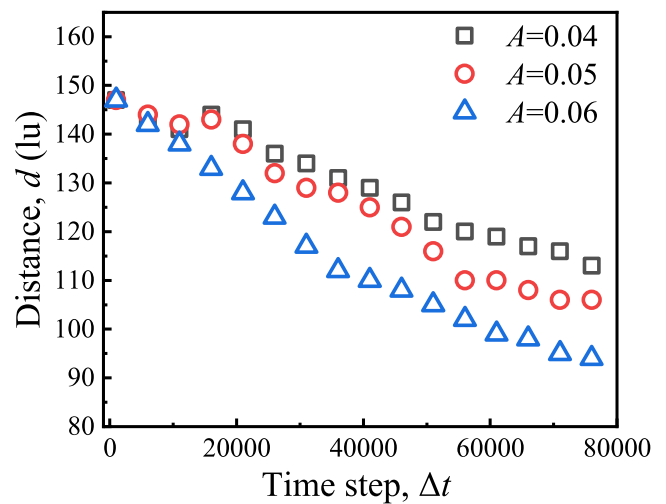
consistent with the experiments. Due to the continuous effects of the ultrasonic waves, the movement of the cavitation bubble and the melting of solid phase proceed (see Fig. 4d and h).

In order to reveal the effects of the cavitation bubble, the evolution of solidification front morphology and temperature field without a cavitation bubble under the effects of the ultrasonic waves are performed. The simulation results are displayed in Fig. 5a-h, showing in density field and in temperature field, respectively. The red and green colors in Fig. 5a-d represent the solid and liquid phases, respectively. It is found that the morphology of solidification front fluctuates due to the temperature change influenced by the periodic ultrasonic pressure and streaming. However, the continuous melting of the solidification front is not observed, which is different from Figs. 2 and 4. Therefore, the existence of the cavitation bubbles has a significant effect on the continuous melting of the solidification front.

Fig. 6 reveals the temperatures on the left and right-hand sides of the cavitation bubble varying with the physical time (see Eq. (4)) for the case of Fig. 4. The inset shows the location of the two measured points. It can be seen that the temperature on the left-hand side of the cavitation bubble fluctuates, while the temperature on the right-hand side increases nonlinearly. This is because the convections appear in the liquid once the ultrasonic source is started, which drive the liquid of high temperature to move to the bubble position in a fluctuating manner, so that the temperature on the left-hand side of the cavitation bubble presents the fluctuations varying with time. Due to the fact that the temperature on the right-hand side is away from the hot region, the temperature rises slowly. In addition, the initialized temperature on the right-hand side of the cavitation bubble is below the liquidus temperature and the position is solid. As the ultrasound works, the temperature gradually increases and exceeds the liquidus temperature, and the solid

phase is melted.

To further understand the interactions between the ultrasound cavitation bubble and the solidification front, a theoretical model proposed by Wang et al. [2] is employed together with the LB simulations. Fig. 7 shows the schematic illustration of the interactions between a cavitation bubble and solidification front in the work of Wang et al. [2], where R is the distance between the solidification interface, and R_0 is the initial distance at $t = 0$ s. f represents a shape factor of the solidification front. The cavitation bubble gradually moves away from the ultrasonic source under the ultrasound effect. As the solidification front melts, R gradually decreases.

The essential equation of the theoretical model is [2].

$$\frac{dR^*}{dt^*} = -k^* \left(\frac{1}{R^*} - k^* - \Delta P^* \right) \tag{20}$$

where R^* and t^* are non-dimensionalized by introducing $R^* = R/R_0$ and $t^* = t/t_k$, in which t_k is computed by $t_k = \frac{R_0^3}{2\alpha_L} \frac{\Delta S_f \cdot LS_H}{C_L \cdot \gamma_{sl}}$. k^* is calculated by $k^* = (4-2R^*)/f$, and ΔP^* is written by $\Delta P^* = \Delta P \bullet R_0/\gamma_{sl}$. ΔP represents the pressure difference induced by cavitation, and γ_{sl} is surface energy of material.

Fig. 8 shows the comparison of the melting distance of the solidification front obtained from the *in situ* experiments, LB simulations, and theoretical predictions from Eq. (20). The points of the green rectangle and red circle represent the experimental and simulated results, respectively, while the blue line is the theoretical prediction. The theoretical model with the influence of cavitation pressure is utilized, due to that the pressure is considered in the present simulation. The model factors obtained from the simulation are listed in Table 2. It is clear that the solidification front shrinks linearly *versus* t^* until R^* approaches 0.21 in simulation (see the red circles). According to the factors in Table 2, the numerical solutions of Eq. (20) are calculated. It is worth noting that R^* of the blue line decreases smoothly with the t^* in Fig. 8. The evolution of simulation is generally identical with the theoretical prediction. In the theoretical model, the pressure induced by ultrasound has an important influence on the movement of the solidification front, while the temperature affected by the flow dominates the evolution of the solid-liquid interface in the LB model. Thus, the temperature changed by flow is also a critical factor besides pressure for the evolution of the interface.

For investigating the influence of ultrasonic intensity, the evolution of the distance between the right boundary and the solidification front varying with time step is simulated, which is shown in Fig. 9. It is revealed in Fig. 9 that the distance decreases with time step, and the larger the intensity, the faster the melting rate. The ultrasonic source with larger intensity induces the stronger liquid flow. Thus, the cavitation bubble moves fast and the temperature exchanges frequently. As a result, the distance traveled by the cavitation bubble increases and the high-temperature flow is easy to approach the right boundary. In addition, we found that the ultrasonic frequency could also influence the melting rate. The preliminary simulation results indicate that the higher ultrasonic frequency, the slower melting rate. The physical mechanism underlying the effects of frequency on melting rate will be investigated in our future work.

5. Conclusions

In the present work, the effects of an ultrasonic cavitation bubble on the melting of solidification front are investigated through *in situ* observation, LB simulation, and theoretical model. In the *in situ* experiment of directional solidification of a SCN-1.65 wt% alloy, the phenomena of solid melting and dendritic fragmentation, caused by the ultrasound cavitation bubbles, are observed. After quantitative validation of the proposed LB model on aspects of comparing the ultrasonic pressure field in liquid, the evolutions of density and temperature in the domain are simulated by the coupled LB model. The movement of the

ultrasound cavitation bubble and the melting of the solidification front are reproduced. The temperatures on the left and right-hand sides of the cavitation bubble are found to increase under the effects of ultrasound. It can be found that the right temperature gradually exceeds the liquidus temperature, which explains the melting of solidification front. Moreover, the simulated results of the melting distance of the solidification front compare well with the theoretical model. The evolution of the melting interface under the different ultrasonic intensities is investigated. The result reveals that the higher ultrasonic intensity, the faster melting rate of the solidification front. On the other hand, since the dendritic solidification microstructure is more ubiquitous than the planar front in the present study, our next work will be the simulation of the evolution of dendrites and bubbles in ultrasound-assisted solidification.

Declaration of Competing Interest

The authors declare that they have no known competing financial interests or personal relationships that could have appeared to influence the work reported in this paper.

Data availability

Data will be made available on request.

References

[1] S. Wang, J. Kang, Z. Guo, T.L. Lee, X. Zhang, Q. Wang, C. Deng, J. Mi, In situ high speed imaging study and modelling of the fatigue fragmentation of dendritic structures in ultrasonic fields, Acta Mater. 165 (2019) 388–397, https://doi.org/10.1016/j.actamat.2018.11.053.

[2] S. Wang, Z.P. Guo, X.P. Zhang, A. Zhang, J.W. Kang, On the mechanism of dendritic fragmentation by ultrasound induced cavitation, Ultrason. Sonochem. 51 (2019) 160–165, https://doi.org/10.1016/j.ultsonch.2018.10.031.

[3] Q. Chen, S. Lin, C. Yang, C. Fan, H. Ge, Grain fragmentation in ultrasonic-assisted TIG weld of pure aluminum, Ultrason. Sonochem. 39 (2017) 403–413, https://doi.org/10.1016/j.ultsonch.2017.05.001.

[4] K. Yasuda, Y. Saiki, T. Kubo, M. Kuwabara, J. Yang, Influence of high-power ultrasonic irradiation on primary nucleation process during solidification, Jpn. J. Appl. Phys. 46 (7B) (2007) 4939–4944, https://doi.org/10.1143/JJAP.46.4939.

[5] Q.-H. Chen, S.-B. Lin, C.-L. Yang, C.-L. Fan, H.-L. Ge, Effect of ultrasound on heterogeneous nucleation in TIG welding of Al–Li alloy, Acta Metallurg. Sin. (Engl. Lett.) 29 (12) (2016) 1081–1088, https://doi.org/10.1007/s40195-016-0483-1.

[6] H. Huang, L. Qin, H. Tang, D. Shu, W. Yan, B. Sun, J. Mi, Ultrasound cavitation induced nucleation in metal solidification: an analytical model and validation by real-time experiments, Ultrason. Sonochem. 80 (2021), 105832, https://doi.org/10.1016/j.ultsonch.2021.105832.

[7] D. Shu, B. Sun, J. Mi, P.S. Grant, A high-speed imaging and modeling study of dendrite fragmentation caused by ultrasonic cavitation, Metall. Mater. Trans. A 43 (10) (2012) 3755–3766, https://doi.org/10.1007/s11661-012-1188-3.

[8] F. Wang, D. Eskin, J. Mi, C. Wang, B. Koe, A. King, C. Reinhard, T. Connolley, A synchrotron X-radiography study of the fragmentation and refinement of primary intermetallic particles in an Al-35 Cu alloy induced by ultrasonic melt processing, Acta Mater. 141 (2017) 142–153, https://doi.org/10.1016/j.actamat.2017.09.010.

[9] B. Wang, D. Tan, T.L. Lee, J.C. Khong, F. Wang, D. Eskin, T. Connolley, K. Fezzaa, J. Mi, Ultrafast synchrotron X-ray imaging studies of microstructure fragmentation in solidification under ultrasound, Acta Mater. 144 (2018) 505–515, https://doi.org/10.1016/j.actamat.2017.10.067.

[10] S. Wang, J. Kang, X. Zhang, Z. Guo, Dendrites fragmentation induced by oscillating cavitation bubbles in ultrasound field, Ultrasonics 83 (2018) 26–32, https://doi.org/10.1016/j.ultras.2017.08.004.

[11] D.Y. Tan, J.W. Mi, High speed imaging study of the dynamics of ultrasonic bubbles at a liquid-solid interface, Mater. Sci. Forum 765 (2013) 230–234, https://doi.org/10.4028/www.scientific.net/MSF.765.230.

[12] T. Nagira, N. Nakatsuka, H. Yasuda, K. Uesugi, A. Takeuchi, Y. Suzuki, Impact of melt convection induced by ultrasonic wave on dendrite growth in Sn–Bi alloys, Mater. Lett. 150 (2015) 135–138, https://doi.org/10.1016/j.matlet.2015.02.069.

[13] Z. Zhang, C. Wang, B. Koe, C.M. Schlepütz, S. Irvine, J. Mi, Synchrotron X-ray imaging and ultrafast tomography in situ study of the fragmentation and growth

dynamics of dendritic microstructures in solidification under ultrasound, Acta Mater. 209 (2021), https://doi.org/10.1016/j.actamat.2021.116796.

[14] Q. Zhang, D. Sun, S. Pan, M. Zhu, Microporosity formation and dendrite growth during solidification of aluminum alloys: modeling and experiment, Int. J. Heat Mass Transf. 146 (2020), https://doi.org/10.1016/j.ijheatmasstransfer.2019.118838.

[15] F. Shan, J. Tu, J. Cheng, D. Zhang, F. Li, Z. Wang, Acoustic field of an ultrasonic cavity resonator with two open ends: experimental measurements and lattice Boltzmann method modeling, J. Appl. Phys. 121 (12) (2017), https://doi.org/10.1063/1.4978013.

[16] F. Shan, X. Guo, J. Tu, J. Cheng, D. Zhang, Multi-relaxation-time lattice Boltzmann modeling of the acoustic field generated by focused transducer, Int. J. Mod. Phys. C 28 (03) (2017), https://doi.org/10.1142/S0129183117500383.

[17] S. Gong, P. Cheng, Lattice Boltzmann simulation of periodic bubble nucleation, growth and departure from a heated surface in pool boiling, Int. J. Heat Mass Transf. 64 (2013) 122–132, https://doi.org/10.1016/j.ijheatmasstransfer.2013.03.058.

[18] P. Yuan, L. Schaefer, Equations of state in a lattice Boltzmann model, Phys. Fluids 18 (4) (2006), https://doi.org/10.1063/1.2187070.

[19] X. Ma, B. Huang, G. Wang, X. Fu, S. Qiu, Numerical simulation of the red blood cell aggregation and deformation behaviors in ultrasonic field, Ultrason. Sonochem. 38 (2017) 604–613, https://doi.org/10.1016/j.ultsonch.2016.08.021.

[20] Z.L. Guo, C.G. Zheng, B.C. Shi, Non-equilibrium extrapolation method for velocity and pressure boundary conditions in the lattice Boltzmann method, Chin. Phys. 11 (4) (2002) 366–374, https://doi.org/10.1088/1009-1963/11/4/310.

[21] M. Hu, C. Sun, H. Fang, M. Zhu, Competitive dendrite growth during directional solidification of a transparent alloy: modeling and experiment, Eur. Phys. J E Soft Matter. 43 (3) (2020) 16, https://doi.org/10.1140/epje/i2020-11941-4.

[22] P. Tin, H. de Groh III, Surface tension and viscosity of succinonitrile–acetone alloys using surface light scattering spectrometer, Int. J. Thermophys. 25 (4) (2004) 1144–1153, https://doi.org/10.1023/B:IJOT.0000038506.26409.7f.

[23] W.K.A. Ludwig, Direct observation of solidification microstructures around absolute stability, Acta Mater. 44 (1996) 3643–3654, https://doi.org/10.1016/1359-6454(95)00448-3.

[24] Q. Zhang, H. Xue, Q. Tang, S. Pan, M. Rettenmayr, M. Zhu, Microstructural evolution during temperature gradient zone melting: Cellular automaton simulation and experiment, Comput. Mater. Sci. 146 (2018) 204–212, https://doi.org/10.1016/j.commatsci.2018.01.032.

[25] T. Walsh, M. Torres, Finite element methods for nonlinear acoustics influids, J. Comput. Acoust. 15 (3) (2007) 353–375, https://doi.org/10.1142/S0218396X0700338X.

[26] A. Modarreszadeh, E. Timofeev, A. Merlen, P. Pernod, Numerical simulation of the interaction of wave phase conjugation with bubble clouds, Int. J. Multiphase Flow 141 (2021), https://doi.org/10.1016/j.ijmultiphaseflow.2021.103638.